Experimental and theoretical studies of particle generation after laser ablation of copper with a background gas at atmospheric pressure

Sy-Bor Wen[a)], Xianglei Mao [a)] , Ralph Greif [b)], Richard E. Russo [a)]

Abstract

Laser ablation has proven to be an effective method for generating nanoparticles; particles are produced in the laser induced vapor plume during the cooling stage. To understand the in-situ condensation process, a series of time resolved light scattering images were recorded and analyzed. Significant changes in the condensation rate and the shape of the condensed aerosol plume were observed in two background gases, helium and argon. The primary particle shape and size distribution were measured using a transmission electron microscope (TEM), a scanning electron microscope (SEM) and a differential mobility analyzer (DMA). The gas dynamics simulation included nucleation and coagulation within the vapor plume, heat and mass transfer from the vapor plume to the background gas, and heat transfer to the sample. The experimental data and the calculated evolution of the shape of the vapor plume showed the same trend for the spatial distribution of the condensed particles in both background gases. The simulated

particle size distribution also qualitatively agreed with the experimental data. It was determined that the laser energy, the physical properties of the background gas (conductivity, diffusivity and viscosity), and the shape of the ablation system (ablation chamber and the layout of the sample) have strong effects on the condensation process and the subsequent sizes, shapes and degree of aggregation of the particles.

---

a) Lawrence Berkeley National Laboratory, Berkeley, CA 94720

b) Department of Mechanical Engineering, University of California, Berkeley, California 94720

Keywords: nanoparticles, laser ablation, condensation, nucleation, coagulation.

Introduction

Laser ablation has proven to be an effective method for producing nanoparticles [1-8]. In contrast to other technologies, no precursors are required to produce particles during laser ablation and nanoparticles can be formed from most materials including materials with complex stoichiometry. In addition, particles generated from laser ablation have a narrow particle size distribution with a variable primary particle size and shape. The flexibility of the experimental setup also allows laser ablation and subsequent particle generation to be performed in vacuum, in background gases and in liquids. In addition to single laser pulse ablation on a single material, parallel (combinatorial) synthesis of nanoparticles with various compositions is achievable with multiple laser pulses on different materials.

Nanoparticles are generated in the laser induced vapor plume during the cooling stage. The particle sizes after laser ablation evolve from the critical radius of homogeneous nucleation and the duration of the particle growth process [9,10]. Both quantities are functions of the cooling rate of the vapor plume. The cooling rate of the vapor plume is generally very fast (>~10,000 K/s) [11-13]. Consequently, the critical radius of the particles generated by homogeneous nucleation is very small (<~10nm), and the duration for particle growth is very short (<0.1s). Therefore, the particles produced during laser ablation are usually small (<100nm) before cluster agglomeration occurs [3]. By adjusting the laser energy, fluence, wavelength, and the type of background gas, the diameters of nanoparticles produced from laser ablation can easily range between ~5 to ~100 nm. For particle sizes less than ~10nm, quantum confinement effects (discrete electron energy levels resulting from the potential well at the boundary of the

nanoparticles) of certain materials also appear [14], which makes laser ablation an attractive method for generating quantum dots.

The size and shape distribution of nanoparticles from laser ablation are generally difficult to control when compared to other technologies. This difficulty results from the complexity of the laser ablation process. The laser induced vapor plume experiences significant changes in size, shape and temperature before and during the condensation process [11-13]. The size, shape and temperature of the vapor plume are complex functions of the laser energy, physical properties of the background gas and the alignment of the ablation system (chamber size and the sample position).

Researchers have attempted to alter the particle properties by changing experimental parameters; e.g. laser fluence and wavelength, pulse duration, carrier gas type, pressure, and flow rate [15-18]. Experiments such as light scattering and photoluminescence have been used for real-time imaging of the particle production process to study the effects of different experimental parameters [5,19,20]. Analyses simulating particle production and the subsequent particle size distribution based on classical nucleation theory also have been carried out [2,3,8] . However, few studies present both experimental and theoretical analyses at the same time which assists in the understanding of particle generation and growth phenomena.

To study the complex phenomena, the present work focuses on the main condensation process when the temperature of the vapor plume is less than the boiling temperature of the sample material. From previous studies [11-13], the time interval when condensation occurs within the vapor plume with a background gas has been determined to be greater than tens of microseconds after the laser pulse; during this time interval the pressure of the vapor plume is close to the background gas pressure. This work excludes

the external shockwave expansion, internal shockwave reflection, and radiative cooling during the first tens of microseconds after the laser pulse.

Both in-situ and external measurements have been used. For the in-situ measurements, light scattering images from a probe beam passing through the vapor plume at different times after the end of the laser pulse were used to monitor the particle condensation process from tens of μs to ~10 *ms* after the laser pulse. From the light scattering images, the regions where significant condensation occurs can be observed. Measurements of the particle size distribution are achieved by transporting the aerosol flow after the laser pulse to a differential mobility analyzer (DMA) and a nanometer aerosol sampler (TSI 3089). The DMA measured the particle number density and the particle size distribution; the nanometer aerosol sampler is used to collect particles on a silicon nitride film. The shape and size of the primary particles on the silicon nitride film were then measured with a transmission electron microscope (TEM) and scanning electron microscope (SEM). He and Ar were used to study the effects of the ambient gas on particle generation.

A theoretical study considering condensation in a cylindrically symmetric vapor plume also was carried out. In the simulation, heat conduction from the vapor plume to both the background gas and to the ablated sample with diffusion of the vapor atoms from the vapor plume to the background gas from tens of μs to ~10 *ms* after the laser pulse were included. Classical nucleation theory was applied to obtain the nucleation rate within the vapor plume. Previous simulations have used specified temperature profiles to determine the condensation within the vapor plume [2,3,8]. In the present work, the condensation processes were coupled with the gas dynamics of the vapor plume and solved simultaneously to obtain the temperature profile and the subsequent particle size distribution. The coagulation of nanoparticles also was included in the simulations. The

simulated particle size distributions are more than five times larger than previous simulations which considered nucleation alone [2,3].

Pure copper was chosen as the sample to continue the sequence of our previous studies [11-13]. In addition, compared to other materials, copper is inexpensive, easy to obtain and prepare for the experimental purpose. From the theoretical point of view, the physical properties of solid and liquid copper (e.g. conductivity, density, and surface tension) are available as functions of temperature. The tabulated physical properties allow a better simulation of the nanoparticle generation process from homogeneous condensation.

Experimental system

The experimental system is shown in Figure 1. A Nd:YAG laser operating at 1064 nm with a 4-ns pulse duration was used as the ablation source. The laser beam was focused using a quartz lens on a copper sample to a spot diameter of ~800 μm. The experiments were performed in an ablation chamber with different background gases (He and Ar). The laser energy was ~100 mJ. A Ti: sapphire femtosecond laser operating at 800 nm with a 100-fs pulse-width which fires at a specified time after the ablation laser was used as the probe beam for generating the scattering images. The 800nm femtosecond probe light was frequency doubled to 400nm before reaching the vapor plume. A camera lens is aligned perpendicular to the probe beam and is used to image the scattering image onto an Intensified Charge-Coupled Device (ICCD) system with 1024×1024 pixels. A delay generator was used to adjust the time between the lasers and the ICCD, which allowed the measuring of scattering images at different times after the end of the laser pulse. The aerosol flow was first connected to a DMA to determine the particle size distribution; then the aerosol flow was conducted to a nanometer aerosol

sampler under the same ablation conditions for collecting the nanoparticles on a silicon nitride film. The particles on the silicon nitride film were then measured with electron microscopes (TEM and SEM) to determine the primary particle size, shape and degree of aggregation. The particle sizes from the microscopes were utilized to verity of the particle size distribution measured from the DMA.

Most of the scattering from particles generated from condensation within the vapor plume are either in the Rayleigh or Mie scattering regimes. The Rayleigh scattering cross section, σ_s, of a single spherical particle is [21]

$$\sigma_s = \frac{128\pi^5}{3}\frac{r^6}{\lambda^4}\left(\frac{\eta^2-1}{\eta^2+2}\right)^2, \text{ for } r <\sim 0.05\lambda \qquad (1)$$

where r is the radius of the particle, λ is the wavelength of the probe beam, and η is the relative refractive index of the particle material with respect to the surrounding gas. For the 400nm wavelength probe beam, Rayleigh scattering occurs for particles with $r < 20nm$. For larger spherical particles for $0.05\lambda < r <\sim 0.8\lambda$ (corresponding to $20nm < r < 320nm$), Mie scattering occurs. The Mie scattering cross section can be expressed as a power series in r/λ as [21]

$$\sigma_s = \frac{128\pi^5}{3}\frac{r^6}{\lambda^4}\left[\frac{\eta^2-1}{\eta^2+2}\left(1+\frac{12\pi^2}{5}\frac{\eta^2-2}{\eta^2+2}\frac{r^2}{\lambda^2}+\ldots\right)\right]^2 \qquad (2)$$

The scattered light intensity is proportional to the product of the scattering cross section and the particle number density. All scattering images were taken on a plane normal to the sample and at 90 degree with respect to the probe beam.

Theoretical analysis

Condensation in the vapor plume starts shortly after the laser pulse. However, since the average temperature of the vapor plume was high and the thermal radiation was strong during the first few microseconds, condensation is limited only in the region close to the contact surface (between the vapor plume and the background gas) where significant cooling occurred. Afterwards, the temperature is lower than ~5500K and conduction and mass diffusion dominate the heat transfer from the vapor plume to the background gas, causing the temperature of the vapor plume to decrease [13].

The analysis focuses on the time when the temperature of the vapor plume is less than ~5000-5500K (for times later than tens of μs after the end of the laser pulse) [13]. When the temperature of the vapor plume is less than the boiling temperature of the sample, homogeneous nucleation can occur within the vapor plume and particles are generated. The size of the particles increases due to condensation of the vapor on the surface of the existing particles along with coagulation between particles (after particle collisions). The nucleation process and single particle growth stop when the temperature of the vapor plume falls below the melting temperature of the sample. The size-dependent melting of small particles was not considered [22]. Afterwards, the particles can agglomerate to form large irregular-shaped particle clusters due to the interaction of van der Waals and electrostatic forces between particles [9]; particle agglomeration was not included in this study.

At the beginning of the simulation, the vapor plume was considered to be hemispherical and at uniform temperature. In addition, the plume was considered to be stationary at the beginning of the simulation. The condensation process was coupled to the gas dynamics of the vapor plume. The presence of the external shockwave and

radiation cooling of the vapor plume were omitted in the current study. These effects are small because the pressure of the vapor plume is close to atmospheric pressure and the temperature of the vapor plume is low (<3000K) during the major condensation process. Detailed studies of both effects and the conditions when they are important have been presented in previous studies [11,12]. After hundreds of μs, cooling of the vapor plume is strongly affected by condensation of the vapor plume due to the release of latent heat. Therefore, cooling and nucleation of the vapor plume were considered simultaneously. Equations of mass, momentum, and energy conservation for the vapor plume, with nucleation theory are the governing equations needed to study the particle condensation process and are given below.

- Continuity equation of the vaporized sample [22]

$$\frac{D(\rho_v)}{Dt} = -\nabla \cdot \vec{j}_v + S_v \tag{3}$$

where $\vec{j}_v$ is the vapor diffusion flux which consists of mass and thermal diffusion as

$$\vec{j}_v = -\rho D_v \nabla \xi_v - \rho D_v \alpha_{v,g} (1-\xi_v) \nabla \ln T = -\rho D_v \nabla \xi_v - D_v^T \nabla \ln T \tag{4}$$

with ξ_v as the vapor mass fraction in gas phase mass, D_v as the binary diffusion coefficient and D_v^T as the thermal (Soret) diffusion coefficient. D_v^T is neglected because thermal diffusion is much smaller than molecular diffusion; S_v is the conversion rate from the vapor to condensed material.

- Continuity equation of the background gas [23,24]

$$\frac{D[\rho_g]}{Dt} = \nabla \cdot \vec{j}_v \tag{5}$$

- Mass conservation of the condensed vapor [23,24]

$$\frac{D(\rho_d)}{Dt} = -S_v \tag{6}$$

- Momentum conservation of the gas region (vaporized sample plus background gas plus the condensed vapor) [23,24]

$$\frac{D(\rho\vec{V})}{Dt} = -\nabla p + \mu_{mix}\nabla^2\vec{V} + \rho\vec{g} + \vec{\chi} \tag{7}$$

where $\rho = \rho_v + \rho_g + \rho_d$; $\vec{V}$ is the velocity field of the gas region; $\vec{\chi}$ is the additional viscous terms as

$$\begin{aligned}\vec{\chi} = &-\nabla\times(\nabla\times\mu_{mix}\vec{V}) + \frac{4}{3}\nabla\mu_{mix}(\nabla\cdot\vec{V}) + \nabla(\vec{V}\cdot\nabla\mu_{mix}) \\ &-\vec{V}\nabla^2\mu_{mix} + \nabla\mu_{mix}\times(\nabla\times\vec{V}) - (\nabla\cdot\vec{V})\nabla\mu_{mix}\end{aligned} \tag{8}$$

with μ_{mix} the average local viscosity of the vapor and the background gas mixture [24].

- Energy conservation of the gas region [23,24]

By including the Dufour effect (diffusion thermo-effect) and neglecting the Ludwig-Soret effect, the energy equation can be expressed as

$$\frac{D(\rho h)}{Dt} = -\nabla\cdot\vec{q} + S_h,\ \vec{q} = \vec{j}_v(h_v - h_g) - K_{mix}\nabla T,\ S_h = L_v S_v \tag{9}$$

with μ_{mix} the average local thermal conductivity of the vapor and the background gas mixture [24].

- Equation of state

$$P = \left(N_v + N_g\right)k_B T \tag{10}$$

where N_v is the local vapor number density and N_g is the local background gas density.

- General dynamic equation (GDE)

The continuous form of the general dynamic equation can be expressed as [9,10]

$$\frac{Dn}{Dt} = -\frac{\partial(Gn)}{\partial v} + I(v^*)\delta(v - v^*) + \frac{1}{2}\int_o^v \beta(v - v_i, v_i) n(v - v_i, t) n(v_i, t) dv_i - n(v,t)\int_o^\infty \beta(v, v_i)\, n(v_i, t) dv_i \tag{11}$$

where the first term on the right-hand side represents the changes of the particle number density in the volume interval v to $v + dv$ due to the condensation rate G; the second term represents the gain of particle number density due to homogenous nucleation with I as the homogeneous nucleation rate and is evaluated from classical nucleation theory as [25]

$$I = \left(\frac{\rho_v p}{m k_B T \rho_l}\right)\left(\frac{2\sigma m}{\pi}\right)^{1/2} \exp\left(\frac{-4\pi\sigma r^{*2}}{3 k_B T}\right) \text{ and } r^* \text{ is critical radius as } r^* = \frac{2\sigma}{\rho_l R T \ln[S]} \tag{12}$$

with S as the supersaturation ratio. The last two terms of Eq. (11) account for the increase and decrease of particle number density due to Brownian coagulation.

Instead of solving the general dynamic equation by sectional methods [26,27], the method of moments was applied [10,28]. The *j*th moment of the particle size distribution is defined as

$$M_j(t) = \int_0^\infty v^j n(v,t) dv \tag{13}$$

By multiplying the GDE with v^j and then integrating from zero to infinity, the differential equation for the *j*th moment is obtained. A number of moment equations can be produced by this method and the problem is not closed. To solve this problem, the relations for the condensation and the Brownian coagulation speeds are specified as functions of particle size and number density [10]. In addition, the particles were assumed to have a log-normal distribution as in most particle generation analyses [9,10]. The log-normal distribution can be expressed as.

$$n(v,t) = \frac{\mathrm{N}}{3\sqrt{2\pi}\ln s}\exp\left[-\frac{\ln^2(v/v_g)}{18\ln^2 s}\right]\frac{1}{v}, \tag{14}$$

where N is the total number of particles, v_g is the average particle volume and σ is the geometric standard deviation.

The vapor plume is considered to be cylindrically symmetric and the simulation domain is shown in Fig. 2. At the beginning of the simulation, the vapor plume was a hemisphere with a radius $r = a$ and $T = T_{init} = 5200K$. The background gas is steady at 1atm and at 300K since the external shockwave is far from the vapor plume and the carrier gas velocity was small in the ablation chamber. Conduction and diffusion from the vapor plume to the background gas are negligible at the beginning of the condensation simulation (~100 μs after the laser pulse). The outermost boundary for the simulation was at $r = b$ and $z = c$, where $b, c >> a$ which corresponds to the large domain of the background gas. The cylindrical solid sample with $r = b$ and $z = -c$ is much larger than the size of the vapor plume. The initial temperature of the solid is the same as the background gas, $T_{amb} = 300K$, except for the portion of the surface that is in contact with the vapor plume (cf. Fig. 2), where the initial boundary temperature was assumed to be the same as the boiling temperature of the sample, T_{boil}. The following assumptions were made:

1. The coalescence time is very small compared to the collision time of the liquid droplets. Liquid droplets attain spherical shapes immediately after sintering with each other.
2. Solid particle aggregation is neglected since the study focused on the determination of

the characteristics of the primary constituent particles.

3. Diffusion of nanodroplets is neglected (Note that $D \propto 1/\sqrt{M}$ and the mass of each droplet is much larger than the carrier gas molecular weight.)
4. Thermphoresis (thermal diffusion) for nanodroplets is neglected in the general dynamic equation (GDE).
5. The velocity of the nanodroplets is the same as the carrier gas (the Reynold numbers of the nanodroplets are much smaller than 1)
6. The conductivity and viscosity contributions of the nanodroplets are neglected in the droplet, vapor, and background gas mixture; droplets are only a small portion of the volume of the mixture.
7. Supersaturation S in Eq. 12 is expressed as $S = p_v / p_{sat}$ which neglects the contribution of the carrier gas. This relation is a good approximation for a vapor-gas mixture at near-atmospheric pressure [29,30].

The small effect that nanodroplets have on the physical properties of the vapor and gas mixture is noted from the following. If all of the vapor with a background gas pressure of 1 atm is converted to nanoparticles of $d \geq 10nm$, the droplet number density is $\leq 0.1\%$ of the total particle number density of the gas mixture (droplets + vapor + background gas) since each droplet contains $\geq 1,000$ atoms. Because of the low number density of the nanodroplets in the mixture, the effects of nanodroplets on the viscosity and thermal conductivity of the flow field are negligible. The boundary conditions for the simulations are listed in appendix.

The calculation domain was divided into small equal size control volumes and the

conservation laws of mass, momentum, energy, and particle number density were applied to each cell to obtain the difference equations for the simulation. The first-order upwind scheme was used for evaluating the fluxes between cells and the implicit algorithm was used in evaluating the physical values for the next time step.

Pure copper was chosen as the sample material for the simulation. Physical properties such as the saturation vapor pressure and surface tension coefficient were considered to be functions of temperature [31].

Results and Discussion

In earilier studies which focused on the particle condensation process with zero (vacuum) or low pressure of the background gas [2,3], the expansion speed and subsequent cooling rate of the vapor plume were very fast. Consequently, particles experienced almost no coagulation before reaching the quenching temperature (i.e. the temperature when nanoparticles stop growing) [2]. For ablation in a background gas at atmospheric pressure, expansion of the vapor plume is confined by the background gas and the vapor plume experiences a slower cooling rate compared to that in a vacuum[1,4,5], which allows significant coagulation among condensed nanodroplets. In addition, the presence of the background gas conducts heat away from the vapor plume and affects the flow pattern of the vapor plume during the condensation process. Both mechanisms have significant effects on particles generated by laser ablation.

From both experimental and simulated results, several important differences have been obtained for copper particle generated from ablation in helium compared to that in argon at one atmosphere. To make a comparison between the condensation processes in

argon and in helium, it is useful to have approximately the same size vapor plume for both cases when the major condensation occurs; i.e. at tens of microseconds after the laser pulse. Ablation with an IR laser ($\lambda = 1064nm$) at E=100mJ and a spot radius ~800 μm produces similar amounts of the vaporized mass in argon and in helium [10,11]. Consequently, the size of the vapor plume after the laser pulse during the condensation process is similar for both background gases. In both argon and in helium, the radius of the vapor plume is $\sim 4mm$ when the temperature of the vapor plume is $\sim 5200K$ [13]. These values were selected as the initial conditions for the condensation simulations.

1. Particle generation process for ablation in Ar and He

For ablation in both background gases, condensation starts near the interface of the vapor plume that is in contact with the background gas, because of the strong heat conduction and mass diffusion between these two regimes. Rapid cooling and the relatively lower density of the vapor plume near the vapor plume-background gas interface compared to that in the bulk of the vapor plume generates smaller particles (d<~10 nm) near the interface (cf. Fig. 3c and 4c). Later, at hundreds of microseconds after the laser pulse (when the temperature of the vapor plume adjacent to the sample surface is much less than the boiling temperature of the sample), significant condensation begins to occur near the sample surface. The higher thermal conductivity of the solid compared to that of the vapor plume effectively removes the latent heat released by the condensation of the vapor plume near the sample. Therefore, the vapor temperature near the sample surface is lower than that of the bulk vapor plume. Furthermore, the condensation of vapor to nanodroplets reduces the vapor atom number density and results

in a lower pressure near the sample, causing a vapor flow towards the sample (Fig. 3b and 4b). Both effects (lower temperature and a supply of vapor toward the sample surface) induce a high condensation rate near the sample. Therefore, the nanodroplet number density is much higher near the sample except for the central region of the vapor plume. The temperature near the center of the vapor plume, compared to the outer region, stays at a higher temperature for a longer time. Consequently, significant coagulation occurs among droplets within this high temperature region, which results in a larger particle size (d~100nm in Ar and d~45nm in He) but lower particle number density (cf. Fig. 5d and 6d) near the center of the vapor plume. The large particles near the center correspond to the strong light scattering measured near the laser spot in Ar and He for times less than ~1ms after the laser pulse (cf. Figs. 7 and 8). For the region of the vapor plume away from the sample and the background gas, medium sized nanoparticles (between d~20 to 50nm) are generated compared to the large particles in the region near the sample and the small particles near the background gas (cf. Figs. 5c and 6c). The medium sized nanoparticles result from the larger critical radius of nucleation and the longer duration of condensation (both of which result from the lower rate of temperature decrease in this region of the vapor plume).

Three major differences were discerned between particles generated in helium compared to these in argon (cf. Fig. 3-8). First, condensation starts and stops earlier in helium than in argon (cf. Fig. 3-8); this is seen in both the scattering images and in the simulation. Second, from both the experiments and the simulation, the nanoparticle sizes produced in helium were smaller than in argon (cf. Figs. 5c and 6c); this was also manifested in the lower scattering intensity measured for ablation in helium. Finally, there was a significant vortex ring present in helium but not in argon in the experiments,

which is seen in both the scattering images and in the simulation (cf. Figs. 6 and 8).

These differences result from the much higher heat conduction and diffusion in helium than in argon, which leads to a faster cooling rate of the vapor plume. The faster cooling rate induces a higher supersaturation ratio in the vapor plume which results in a smaller critical radius for homogeneous nucleation. Also, the faster cooling rate reduces the time duration for the condensation process after the particles have been generated from nucleation (i.e. the time interval when the temperature of the vapor plume is less than the boiling temperature but more than the melting temperature of the sample). Both the smaller critical radius of the nuclei and the shorter time duration for the condensation process result in smaller nanoparticles for ablation in helium. Furthermore, because of the higher energy transfer rate from the vapor plume to the background gas for ablation in helium, the background gas near the vapor plume is heated more efficiently in helium. This higher temperature results in a higher pressure of the helium background gas near the vapor plume, which causes the helium to move toward the sample surface (significant condensation near the sample surface results in a low pressure region). A vortex ring is generated during the condensation process in helium. The higher viscosity (higher viscous force) of helium compared to argon effectively enlarges the region affected by the vortex ring. The presence of the strong vortex ring in helium also enhances the mass transfer between the vapor plume and the background gas, further increasing the cooling rate of the vapor plume and reducing the particle sizes from condensation (cf. Figs. 6 and 8). The presence of a vortex ring in He not only changes the particle size distribution, but also affects the spatial particle distribution. The vortex ring carries nanoparticles away from the sample surface. For ablation in helium, most nanoparticles are transported away from the sample by the carrier gas rather than falling back to the sample surface as seen

for ablation in argon. These data are consistent with experiments showing much less deposition around the crater for ablation in He than in Ar (Fig. 9) [32].

2. Particle size distribution for ablation in Ar and He

The particle size distributions for ablation in Ar and He were measured with a DMA which detects particles from d~10 to 300nm (Fig. 10). For ablation in Ar, the particle size distribution is close to a log-normal distribution with a maximum at ~28nm. For ablation in He, the DMA was unable to determine the particle size distribution because a significant portion of the particles have diameters less than 10nm.

The aerosol flow was also channeled to a nanometer aerosol sampler and then collected on a silicon nitride film. For ablation in argon, most of the particles had a diameter between d~20 to 50nm (Fig. 11); particles were spherical or cubic shapes. Some of the particles aggregated to form large agglomerations. Some crystal facets were observed in TEM images of the nonspherical particles and agglomerations which are considered to have a crystalline structure. For ablation in helium, all of the particles were between d~5 to 10nm, Fig. 12, and most were spheres. These TEM and SEM images in both argon and helium demonstrate that most particles counted by the DMA were single particles rather than agglomerations.

Particle size distributions were also determined from the simulations for ablation in Ar and He. By integrating throughout the entire simulation domain, the particle size distributions after single pulse ablation were obtained (Fig. 13). In agreement with experiments, more large particles were produced for ablation in Ar than in He. However, the shape of the simulated primary particle size distribution was not in good agreement

with the experimental data, especially for ablation in Ar. In the simulation, the peak of the particle size distribution was at d~3nm for ablation in Ar with a secondary hump at d~30nm; in the experiment, the particle size was close to a log-normal distribution with a single peak at d~30nm. Besides the simplifications in the simulation, this discrepancy in the simulated and experimental particle size distributions also results from the difference between the particles that are present at the end of condensation and those particles that actually reach the DMA. The simulated results predict the particle size distribution at the end of the condensation process in the ablation chamber. However, not all of the condensed particles reach the DMA; a portion of the condensed nanoparticles deposits on the sample (Fig. 9) which leads to a measured result that is less than the actual particles at the end of the condensation process. In addition, a significant portion of small nanoparticles (d<10nm) also deposit on the walls of the ablation chamber and on the tubing to the DMA [33]; this reduced the first peak of the simulated particle size distribution (which occurs at d~3nm) in the DMA measurements. When the effects of Brownian motion (diffusive loss) and gravity were considered on the "transport efficiency" in the simulation [34-36], the simulated particle size distribution resulted in better agreement with the experimental data (Fig. 13). From both the experimental and analytical results, the particle size distributions were polydisperse for both ablation in Ar and He.

3. Effects of the laser input on the condensation process

The size of the condensed particles in the vapor plume is related to the laser energy. Lower laser energy generates a smaller vapor plume. The energy transfer rate from the vapor plume to the background gas and to the sample is proportional to the surface area

of the vapor plume ($\propto r^2$); the total thermal energy stored in the vapor plume is proportional to the volume of the vapor plume ($\propto r^3$). Therefore, the rate of the temperature decrease of the vapor plume is proportional to r^{-1}. Both the critical radius of the nuclei from homogeneous nucleation and the time duration available for the growth of nanoparticles in the vapor plume are reduced in a smaller vapor plume with its faster cooling rate. The simulation is in agreement with these data; when the initial vapor plume size decreases from $r = 4mm$ to $2mm$ the time required for the temperature of the entire vapor plume to be lower than the melting temperature of the sample decreases from 4.1 to 1.7ms in argon and from 1.2 to 0.5ms in helium. There is a ~40% decrease in the maximum condensed particle size when the vapor plume size decreases from $r = 4mm$ to $2mm$ for both background gases (argon and helium).

The decrease in the particle size for lower laser energy was also seen in the scattering images. Very little or no light scattering was detected for smaller ablation laser energies (<50mJ for the IR ablation laser with the probe laser beam at $\lambda = 400nm$); this is a result of a significant reduction in Rayleigh and Mie scattering cross sections, which are proportional to $\sim r^6$ [21].

4. Agglomeration of solid nanoparticles

The simulation stops when the temperature of the vapor plume is lower than the melting temperature of the sample (when condensation stops in the vapor plume); this time occurs from 1 to $3ms$ after the end of the laser pulse. The images show that the scattering intensity from the vapor plume continues to increase long after the end of the condensation process within the vapor plume (the measurements stop at $\sim 15ms$ after the end of the laser pulse). This increase in scattering intensity is a consequence of the

agglomeration of solid nanoparticles after the condensation process (Figs. 11 and 14). The solid nanoparticles aggregate, due to the van der Waals and electrostatic forces, to form larger particle agglomerates after colliding with each other. The size of the agglomerates continues to increase with time after the laser pulse until a stable size and shape is reached. The simulation does not include the agglomeration process for solidified nanoparticles. Agglomeration mechanisms which are affected by the force field of the condensation environment have been extensively studied recently [12]. Agglomerated particles can be found for both ablation in Ar and He (Fig. 14).

5. Comparison between simulation and experiment

In the simulation, the width of the sample was considered to be semi-infinite. However, the sample size in the experiment was about twice the diameter of the vapor plume. This relatively small sample size (compared to the size of the vapor plume) induced an edge effect that is shown in figure 15 (in argon) during the condensation process. A large, non-symmetrical vortex ring was generated near the edge of the sample at the bottom of the vapor plume when the laser spot was adjacent to the edge of the sample for ablation in both Ar and He; this edge effect was not present in the simulation which considered an infinitely wide sample. The origin of the vortex ring (which is different from the vortex ring for ablation in helium with a semi-infinite sample) results from the inward flow of the background gas from the edge to the low pressure region around the laser spot. The strength of the vortex ring is inversely proportional to the distance between the laser spot and the edge of the sample because the sample surface provides an additional resistance to the inward flow.

This edge effect also influences the motion of the vortex ring for ablation in helium.

In the simulation for ablation in helium (which is also for an infinite width), the vortex ring is present and keeps moving upward during condensation (cf. Fig. 16). However, the scattering images (in helium) actually show a quasi non-moving vortex ring (which moves upward or along the sample surface with a much slower speed than the predictions) and persists long after the end of condensation (cf. Fig. 6). The edge of the sample provides an additional drag force retarding the motion of the vortex ring.

Another important difference between the simulation and the experiments is the finite size of the ablation chamber. A no-slip boundary condition at the wall of the finite ablation chamber results in a different flow pattern and in the subsequent cooling rate of the vapor plume than is obtained from the simulation which is for an infinitely large region for the background gas. This difference also is one of the possible origins of the deviation between the particle size distributions predicted and measured.

It is also noted that the experimental and the simulated background gas conditions are different. In the experiment, the background gas was supplied from a small tube to the ablation chamber. The background gas flow does not always carry away the nanoparticles generated from the previous laser pulse before another laser pulse is initiated. Therefore, nanoparticles which accumulate in the background gas of the chamber can provide initial nuclei for the vapor plume condensation, which changes the condensation conditions. Residual nanoparticles from previous pulses also can change the shape and size of solid clusters from agglomeration. This nanoparticle accumulation in the background gas is seen in the scattering images, especially for the experiments in helium (cf. Fig. 8). A uniform light band appears in the background of the scattering images which has the same width as the probe beam after several pulses in the same chamber (the laser repetition rate was ~30 seconds per laser pulse). The band results from the interaction of

the accumulated nanoparticles (which are generated from the previous laser pulse) with the probe beam. The strength of the light band is reduced when the flow rate of the gas to the ablation chamber is increased.

Conclusions

The particle condensation process and the subsequent particle size distribution showed significant differences for ablation in argon and helium. Compared to ablation in argon, condensation starts and stops earlier for ablation in helium, and the final particle sizes for ablation in helium are smaller than that in argon (<10nm vs. ~30nm). The simulation demonstrates the differences as a consequence of the much higher thermal conductivity of helium (ten times greater than that of argon). Consequently, the vapor plume cools faster for ablation in helium. The faster cooling rate induces a higher supersaturation ratio and a shorter condensation duration which result in smaller particles from condensation.

In addition to the type of background gas, the amount of laser energy and the arrangement of the sample in the ablation chamber influence the cooling rate of the vapor plume and the subsequent particle size distribution. The cooling rate is inversely proportional to the size of the vapor plume and the size of the vapor plume decreases monotonically with the laser energy. Therefore, the lower laser energy results in smaller particle sizes produced from condensation. The cooling rate also depends on the location of the laser input on the sample. For example, a vortex ring appears in the vapor plume when ablation occurs near the edge of the sample. The vortex ring improves the heat transfer and cooling rate of the vapor plume.

The study showed the particle size distribution as functions of background gas, laser

energy, and laser input location. These data can be utilized for design of laser ablation systems in order to produce a more controlled distribution of particles. Further studies will emphasize on controlling the shape of the primary particle size distribution; e.g. monodispersive vs. polydispersive. In addition, the transport of the particles from the ablation site to the collection site is an important issue of the future studies.

Acknowledgement

This work was supported by the U.S. Department of Energy, Office of Basic Energy Sciences, Chemical Sciences Division at the Lawrence Berkeley National Laboratory (LBNL) under contract number DE-AC02-05CH11231. The authors acknowledge support of the National Center for Electron Microscopy at LBNL. The authors are also pleased to acknowledge the helpful discussions with Howard Baum of NIST, Paul Berdahl and Xiangyun Song of LBNL.

References

[1] A. A. Puretzky, D. B. Geohegan, H. Schittenhelm, X. D. Fan and M. A. Guillorn, Time-resolved diagnostics of single wall carbon nanotube synthesis by laser vaporization, Applied Surface Science 197, 552-562, 2002.

[2] M. Kuwata, B. Luk'yanchuk and T. Yabe, Nanocluster formation within the vapor plume, produced by nanosecond-laser ablation: effect of initial density and pressure distribution, Jpn. J. Appl. Phys., 40, 4262-4268, 2001.

[3] T. Ohkubo, M. Kuwata, B. Luk'yanchuk and T. Yabe, Numerical analysis of nanocluster formation within ns-laser ablation plume, Appl. Phys. A, 77, 271-275, 2003.

[4] T. Makimura, T. Mizuta and K. Murakami, Formation dynamics of silicon nanoparticles after laser ablation studied using plasma emission caused by second-laser decomposition, Appl. Phys. Letters, 76, 1401-1403, 2000.

[5] Y. Nakata, J. Muramoto, T. Okada and M. Maeda,Particle dynamics during nanoparticle synthesis by laser ablation in a background gas, J. Appl. Phys, 91, 1640-1643, 2002.

[6] S. R. Franklin and R. K. Thareja, Simulation of cluster formation in laser-ablated silicon plumes, J. Appl. Phys., 97, 123303, 2005

[7] H. R. Kuhn, J. Koch, R. Hargenroder, K. Niemax, M. Kalberer and D. Gunther, Evaluation of different techniques for particle size distribution measurements on laser-generated aerosols, J. Analytical atomic spectrometry, 20, 894-900 2005.

[8] R. Hergenroder, A model for the generation of small particles in laser ablation ICP-MS, Journal of Analytical Atomic Spectrometry 21, 1016 (2006)

[9] S. K. Friedlander, Smoke, Dust, and Haze: Fundamentals of aerosol dynamics, 2nd

edition, Oxford University Press, New York, 2000.

[10] S. E. Pratsinis and K. S. Kim, Particle Coagulation, Diffusion and Thermophoresis in Laminar Tube Flows, Journal of Aerosol Science, 20, 101-111, 1989.

[11] S. B. Wen, X. Mao, R. Greif and R. E. Russo, Study of the expansion of the vapor plume generated by laser ablation with a background gas – Part A. Theoretical Analysis, Journal of Applied Physics, 2006, accepted for publish.

[12] S. B. Wen, X. L. Mao, R. Greif and R. E. Russo, Study of the expansion of the vapor plume generated by laser ablation with a background gas – Part B. Experimental Analysis, Journal of Applied Physics, 2006, accepted for publish.

[13] S. B. Wen, X. L. Mao, R. Greif and R. E. Russo, Radiative cooling of laser ablated vapor plumes: experimental and theoretical analyses, Journal of Applied Physics 100, 053104 (2006).

[14] T. Takagahara and K. Takeda, Physical Review B **46**(23), 15578 (1992).

[15] A. A. Gorbunov, R. Friedlein, O. Jost, M. S. Golden, J. Fink, and W. Pompe, Appl. Phys. A 69, S593 (1999).

[16] M. Tudasaka, R. Yamada, N. Sensui, T. Wilkins, T. Ichihashi, and S. Iijima, J. Phys. Chem. B 103, 6224 (1999).

[17] O. Jost, A. A. Gorbunov, J. Moller, W. Pompe, A. Graft, R. Friedlein, X. Liu, M. S. Golden, and J. Fink, Chem. Phys. Lett. 339, 297 (2001).

[18] A. S. Bandow, S. Asaka, Y. Saito, A. M. Rao, L. Grigorian, E. Richter, and P. C. Eklund, Phys. Rev. Lett. 80, 3779 (1998).

[19] J. Muramoto, T. Inmaru, Y. Nakata, T. Okada, and M. Maeda, Appl. Phys. A 69, S239 (1999).

[20] T. Ikegami, S. Ishibashi, Y. Yamagata, and K. Ebihara, J. Vac. Sci. Technol. A 19(4),

1304 (2001).

[21] R. Siegel and J. Howell, Thermal radiation heat transfer, 4ed, Taylor & Francis, 2001.

[22] K. K. Nanda, Eur. J. Phys. 19, 471 (1998).

[23] D. F. Banse, Theoretical study of particle/droplet activation and growth in the Leipzig Aerosol and Cloud Interaction Simulator (LACIS), Diploma Thesis, University of Leipzig, Leipzig, Germany, 2003.

[24] A. F. Mills, Mass Transfer, Prentice Hall, Upper Saddle River, NJ, 2001.

[25] V. P. Carey, Liquid-Vapor Phase-Change Phenomena, Taylor & Francis, 1992.

[26] F. Gelbard and J. H. Seinfeld, Simulation of multicomponent aerosol dynamics, J. Colloid Interf. Sci., 78, 485-501, 1980.

[27] K. E. J. Lehtinen and M. Kulmala, A model for particle formation and growth in the atmosphere with molecular resolution in size, Atmos. Chem. Phys., 3, 251-257, 2003.

[28] S. L. Girshick, Particle nucleation and growth in thermal plasmas, Plasma Sources Sci. Technol., 3, 388-394, 1994.

[29] P. Peeters, J. J. H. Gielis, and M. E. H. van Dongen, Journal of Chemical Physics, 117(12), 5647 (2002)

[30] C. C. M. Luijten and M. E. H. can Dogen, Journal of Chemical Physics, 111(18), 8524 (1999)

[31] T. Iida and and R. I. L.Guthrie, The physical properties of liquid metals, Oxford University Press, New York, 1988.

[32] I. Horn and D. Gunther, Applied Surface Science 208(1-4), 144 (2003).

[33] P. Arrowsmith ands. K. Hughes, Entrainment and Transport of Laser Ablated Plumes for Subsequent Elemental Analysis, Applied Spectroscopy 42(7), 1231 (1988).

[34] P. Arrowsmith and S. K. Hughes, Applied Spectroscopy, 42(7), 1231 (1988)

[35] S. H. Jeong, O. V. Borisov, H. H. Yoo, X. L. Mao and R. E. Russo, Anal. Chem., 71, 5123 (1999)

[36] P. G. Gormley and M. Kennedy, Proc. Royal Irish Acad., 52A, 163 (1949).

Nomenclature

B_{1-4}	Constants defined in Eq. (14), (15), (19) and (20) separately
D_v	binary diffusion coefficient
D_v^T	thermal (Soret) diffusion coefficient
G	condensation rate
h	enthalpy
I	homogeneous nucleation rate
$\vec{j}_v$	vapor diffusion flux
K	thermal conductivity
k_B	Boltzmann constant
M_j	jth moment of of the particle size distribution
N	total number of particles
N	atomic number density
n	particle size distribution
P	pressure of the gas phase region
$\vec{q}$	heat flux
r^*	Critical radius of the liquid droplet during homogenous nucleation
S	supersaturation ratio
S_v	conversion rate from the vapor to condensed material
s	geometric standard deviation
T	temperature
$\vec{V}$	velocity field of the gas phase region
v	particle volume
v_g	average particle volume
β_{FM}	Brownian collision frequency
$\vec{\chi}$	additional viscous term defined in Eq. (8)
Φ_{ij}	A dimensionless functions defined in Eq. (8)
η	relative refractive index of the particle material with respect to the surrounding gas

λ	wavelength of the probe beam
μ_{mix}	Viscosity of the gas and vapor mixture
ρ	total gas phase mass density
ρ_d	droplet mass density
ρ_g	gas mass density
ρ_l	melted sample mass desnity
ρ_v	vapor mass density
σ	surface tension of the melted sample
σ_s	scattering cross section
ξ_v	vapor mass fraction in gas phase mass

Subscript

c	continuum regime
d	condensed droplet
FM	free molecule regime
g	background gas
v	vaporized sample

List of Figures

Figure 7. Rayleigh scattering images of condensed particles from the copper vapor plume in argon at different time after the laser pulse. ($E = 100mJ, \lambda = 1064nm, d \sim 800nm$)

Figure 8. Rayleigh scattering images of condensed particles from the copper vapor plume in helium at different time after the laser pulse. ($E = 100mJ, \lambda = 1064nm, d \sim 800nm$)

Figure 9. Craters after 50 laser pulses for ablation in argon and helium

Figure 10. Particle size distributions measuring by a DMA (digital mobility analyzer) for ablation in Ar and He.

Figure 11. SEM images of particles collected on a SiN_4 film for ablation in argon

Figure 12. TEM images of particles collected on a SiN_4 film for ablation in helium

Figure 13. Simulated particle size distributions for ablation (a) in Ar and (b) in He.

Figure 14. Agglomerated particles collected on a SiN_4 for ablation in (a) argon (TEM image) and (b) helium (SEM image).

Figure 15. Rayleigh scattering images of condensed particles from the copper vapor plume in argon at 1ms after the laser pulse when the laser spot is close to the edge of the sample.

Figure 16. The evolution of the vortex ring in the vapor plume for the ablation in helium (a) 0.7ms after the laser pulse (b) 1.2ms after the laser pulse (c) 2.0ms after the laser pulse

Appendix

Boundary conditions used in the simulation of the condensation process of the laser induced vapor plume are listed as follows.

1. V_r

$V_r = 0$ at r=0 from mass conservation; $\frac{\partial V_r}{\partial z} = 0$ at r=b; $V_r = 0$ at z=0 from the non-slip boundary condition; $\frac{\partial V_r}{\partial z} = 0$ at z=c

2. V_z

$\frac{\partial V_z}{\partial r} = 0$ at r=0 from momentum conservation; $\frac{\partial V_r}{\partial z} = 0$ at r=b; $V_z = 0$ at z=0 from the non-slip boundary condition; $\frac{\partial V_z}{\partial z} = 0$ at z=c

3. p

$\frac{\partial p}{\partial r} = 0$ at r=b and $\frac{\partial p}{\partial z} = 0$ at z=c. Also, from momentum conservation in the r direction at the symmetric center, an additional condition $\frac{\partial p}{\partial r} = 0$ at r=0 can be obtained.

(The momentum equation in the r direction for the cylindrically symmetric condition is

$$\rho\left(\frac{\partial V_r}{\partial t} + V_r\frac{\partial V_r}{\partial r} + V_z\frac{\partial V_r}{\partial z}\right) = -\frac{\partial p}{\partial r} + \mu\left(\nabla^2 V_r - \frac{V_r}{r^2}\right). \quad (15)$$

Since V_r =0 at r=0 , then $\frac{\partial V_r}{\partial z}$ =0 at r=0 . In addition, with V_r =0 at r=0, $\nabla^2 V_r - \frac{V_r}{r^2} = \frac{1}{r}\frac{\partial}{\partial r}\left(r\frac{\partial V_r}{\partial r}\right) + \frac{\partial^2 V_r}{\partial z^2} - \frac{V_r}{r^2} \approx \left.\frac{\partial V_r}{\partial r}\right|_{r=0} / r - \left.\frac{\partial V_r}{\partial r}\right|_{r=0} / r = 0$ according to a Taylor series expansion at r=0. Therefore, the RHS and the second term of LHS of (13) are

both equal to zero, which results in $\frac{\partial p}{\partial r}=0$ at r=0.)

4. ρ_g, ρ_v, ρ_d

From mass conservation at r=0, the mass flux at r=0 should be zero for the background gas (which diffuses toward the vapor plume), for the vapor (which diffuses to the background gas), and for the condensed droplet from the vapor plume. With $V_r = 0$ at r=0, the above condition at r=0 is equal to

$$\frac{\partial\left(\frac{\rho_g / M_g}{\rho_g / M_g + \rho_v / M_v + \rho_d / M_d}\right)}{\partial r} = \frac{\partial\left(\frac{\rho_v / M_v}{\rho_g / M_g + \rho_v / M_v + \rho_d / M_d}\right)}{\partial r} = \frac{\partial\left(\frac{\rho_d / M_d}{\rho_g / M_g + \rho_v / M_v + \rho_d / M_d}\right)}{\partial r} = 0.$$

With $\frac{\partial p}{\partial r}=0$ at r=0 and the equation of state, $\frac{\partial\left(\rho_g / M_g + \rho_v / M_v + \rho_d / M_d\right)}{\partial r} = 0$ at r=0. Combining the above four relations, we have $\frac{\partial \rho_g}{\partial r} = 0$, $\frac{\partial \rho_v}{\partial r} = 0$, and $\frac{\partial \rho_d}{\partial r} = 0$ at r=0. At the sample surface, $\rho_v = \rho_{v,sat}$. Also, from the similar mass conservation relation at z=0, we have

$$\frac{\partial\left(\frac{\rho_g / M_d}{\rho_g / M_g + \rho_v / M_v + \rho_d / M_d}\right)}{\partial z} = \frac{\partial\left(\frac{\rho_v / M_v}{\rho_g / M_g + \rho_v / M_v + \rho_d / M_d}\right)}{\partial z} = \frac{\partial\left(\frac{\rho_d / M_d}{\rho_g / M_g + \rho_v / M_v + \rho_d / M_d}\right)}{\partial z} = 0.$$

The boundary conditions for ρ_g, ρ_v, and ρ_d at r=b are $\frac{\partial \rho_g}{\partial r} = 0$, $\frac{\partial \rho_v}{\partial r} = 0$, and $\frac{\partial \rho_d}{\partial r} = 0$; at z=c are $\frac{\partial \rho_g}{\partial z} = 0$, $\frac{\partial \rho_v}{\partial z} = 0$, and $\frac{\partial \rho_d}{\partial z} = 0$

5. T

$T = T_2$ at r=b and z=c; $\frac{\partial T}{\partial r} = 0$ at r=0 from the energy conservation;.

$-k_v \left.\frac{\partial T}{\partial z}\right|_{z=0,g} = -k_s \left.\frac{\partial T_s}{\partial z}\right|_{z=0,s}$ and $T = T_s$ at z=0.

6. T_s

$T_s = T_2$ at r=b and z=c; $\dfrac{\partial T_s}{\partial r} = 0$ at r=0 from the energy conservation;.

$$-k_v \left.\frac{\partial T}{\partial z}\right|_{z=0,g} = -k_s \left.\frac{\partial T_s}{\partial z}\right|_{z=0,s} \quad \text{and} \quad T = T_s \quad \text{at } z=0.$$

7. M_0, M_1, M_2

$$\frac{\partial M_0}{\partial r} = \frac{\partial M_1}{\partial r} = \frac{\partial M_2}{\partial r} = 0 \quad \text{at } r=b; \quad \frac{\partial M_0}{\partial z} = \frac{\partial M_1}{\partial z} = \frac{\partial M_2}{\partial z} = 0 \quad \text{at } z=c$$

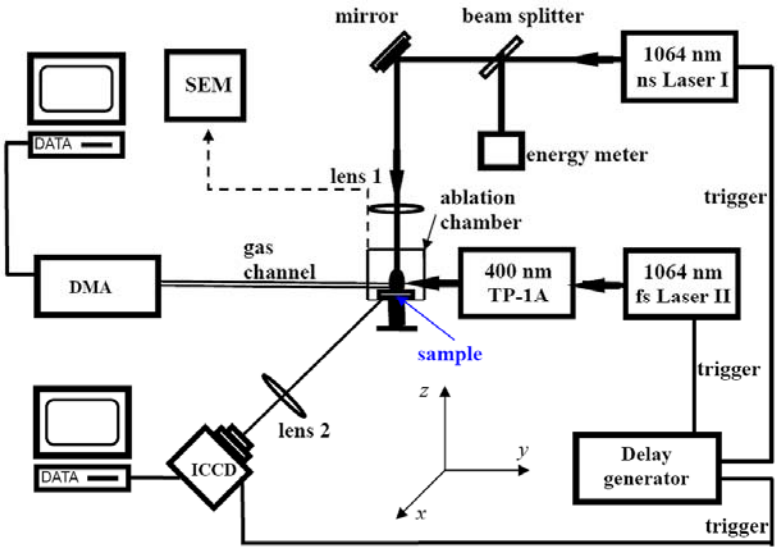
mirror
beam splitter
1064 nm
ns Laser I
SEM
DATA
energy meter
lens 1
ablation
chamber
trigger
gas
channel
DMA
400 nm
TP-1A
1064 nm
fs Laser II
sample
trigger
z
lens 2
ICCD
DATA
y
Delay
generator
x
trigger

Figure 1.

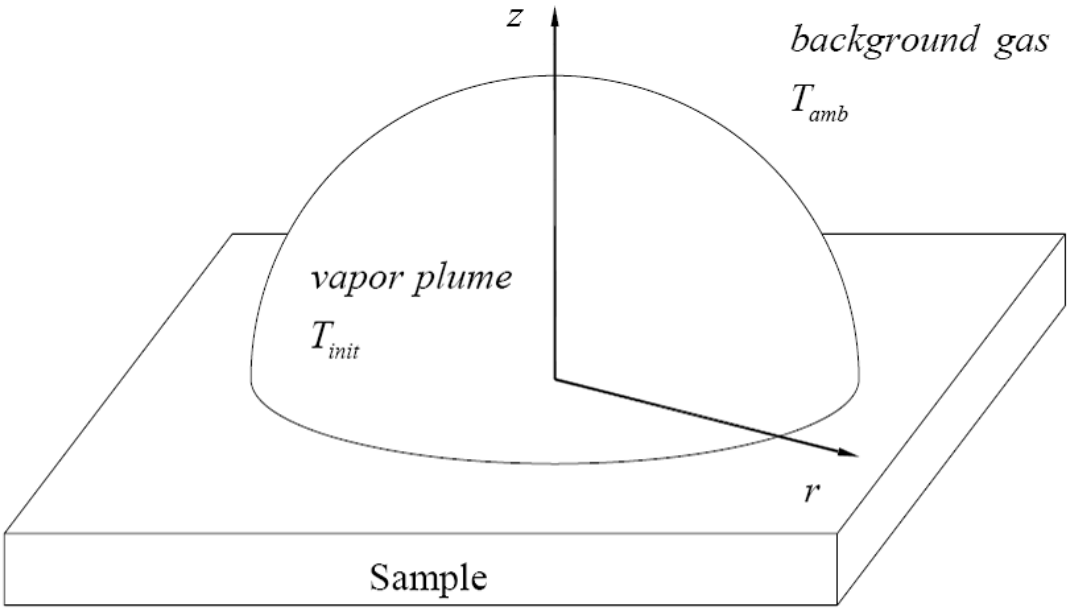

Figure 2

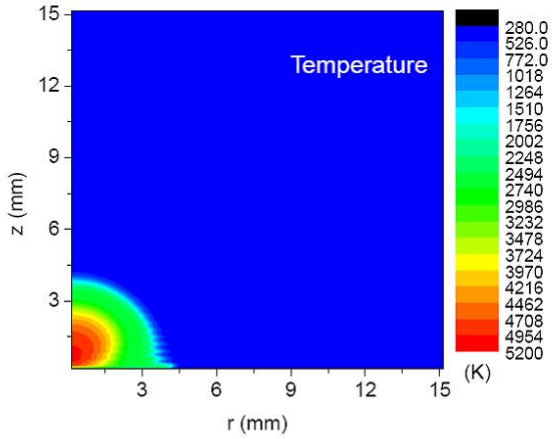

(a)

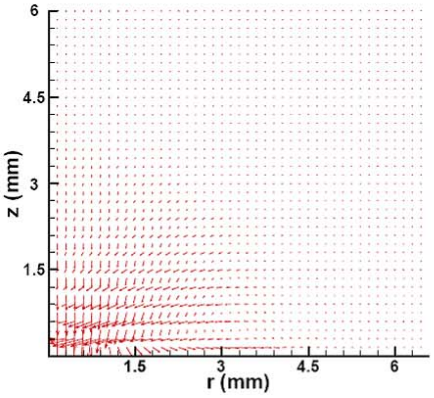

(b)

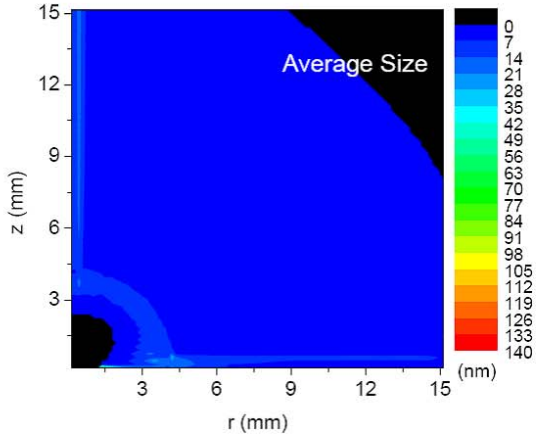

(c)

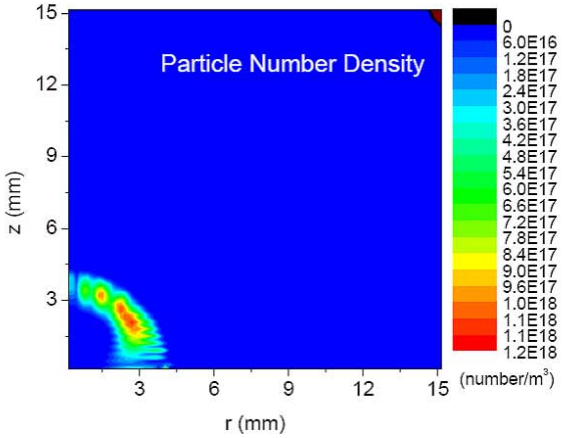

(d)

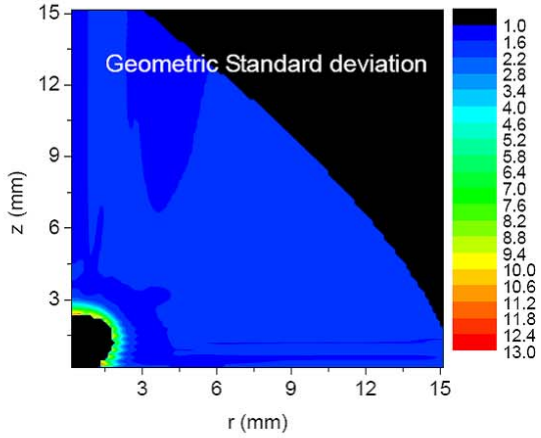

(e)

Figure 3

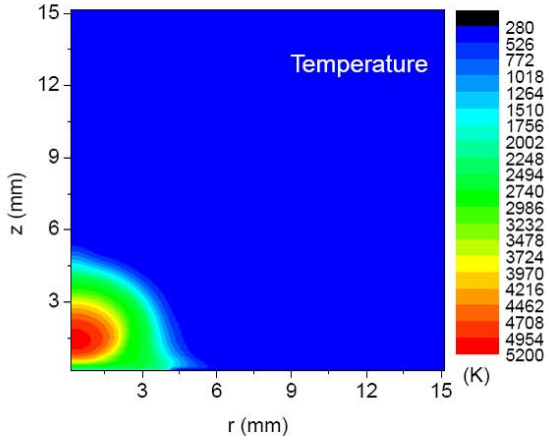

(a)

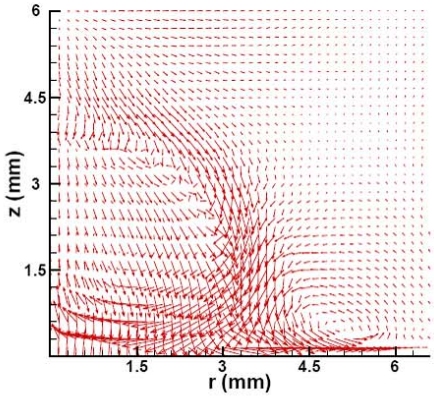

(b)

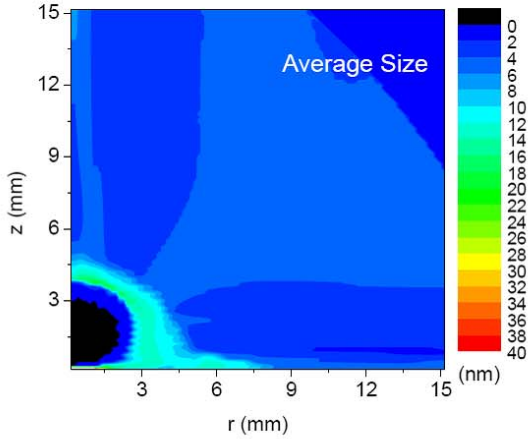

(c)

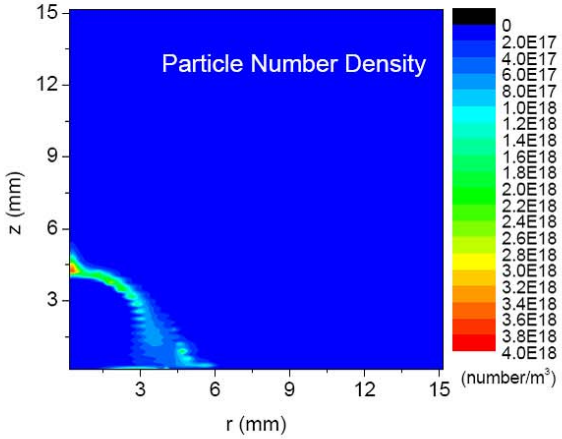

(d)

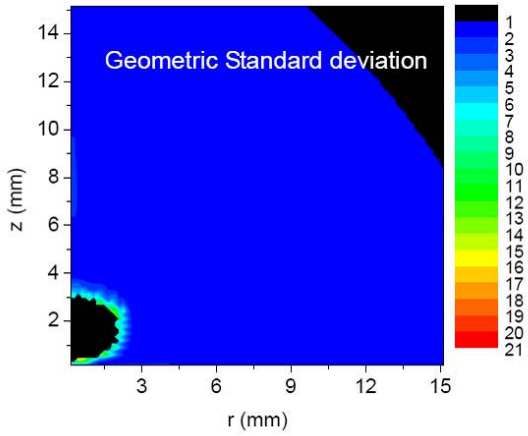

(e)

Figure 4

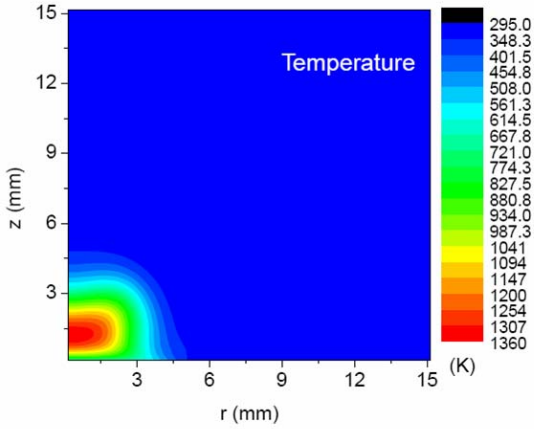

(a)

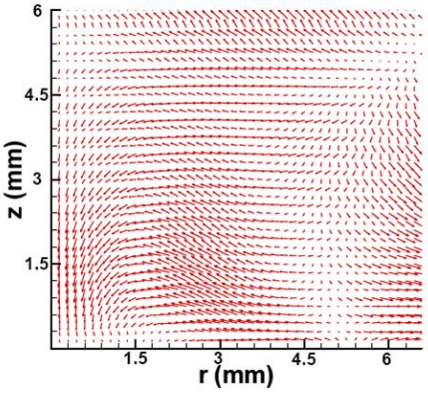

(b)

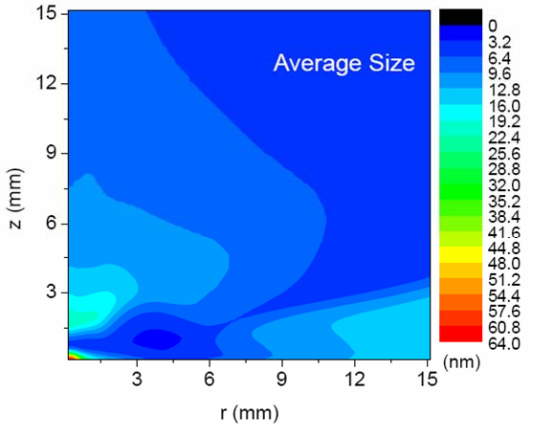

(c)

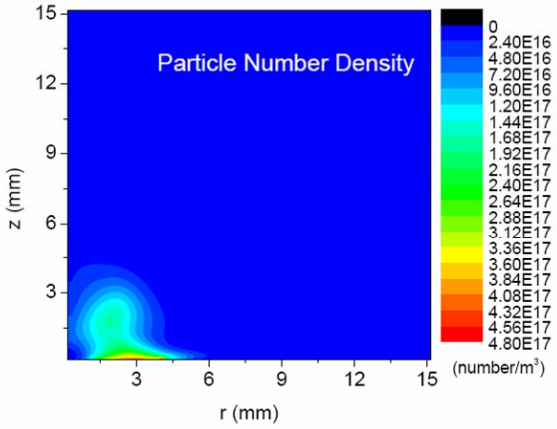

(d)

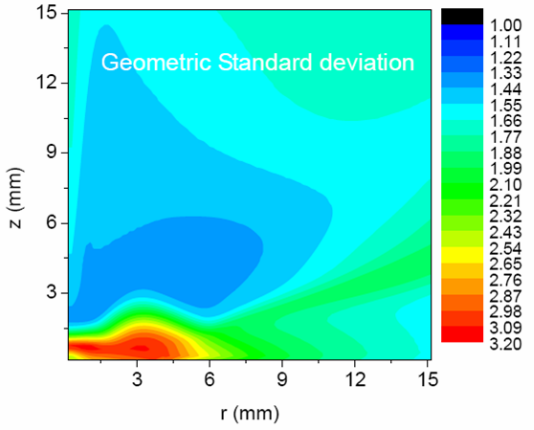

(e)

Figure 5

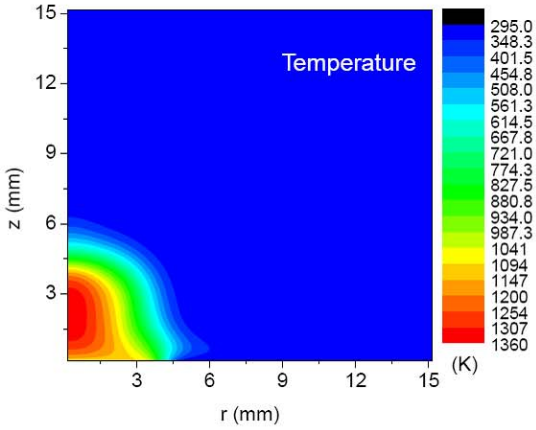

(a)

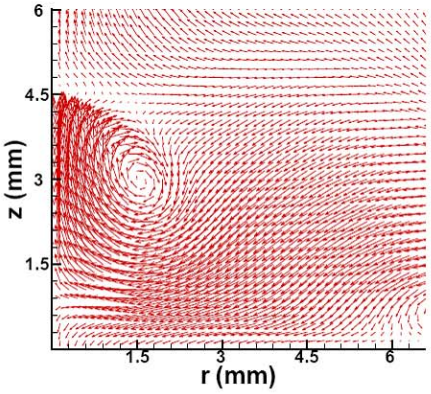

(b)

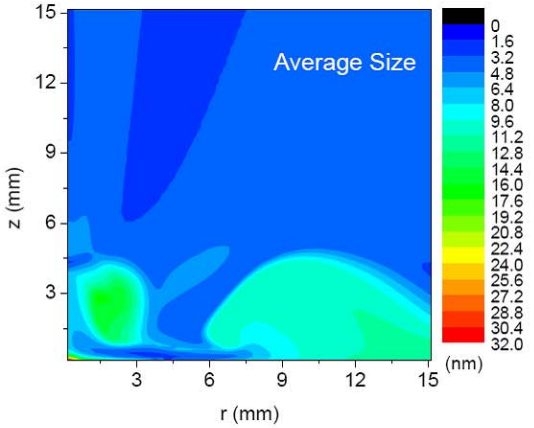

(c)

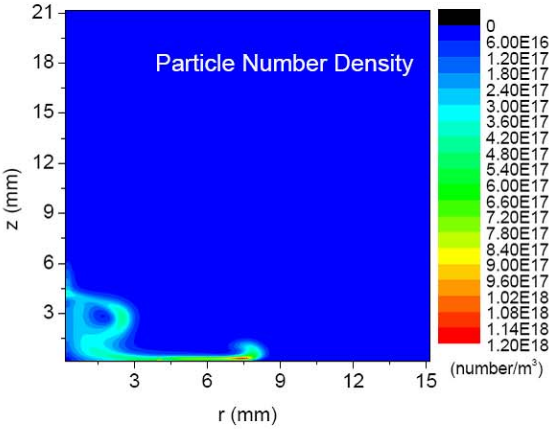

(d)

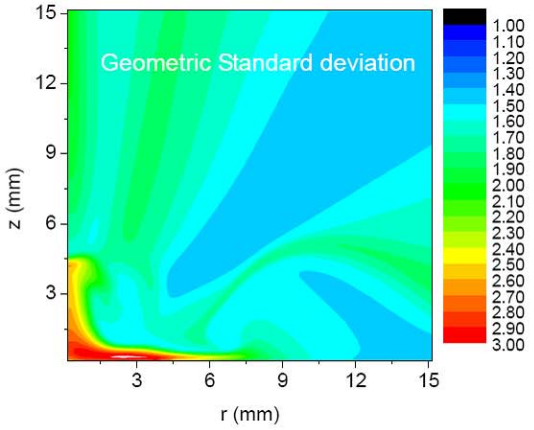

(e)

Figure 6

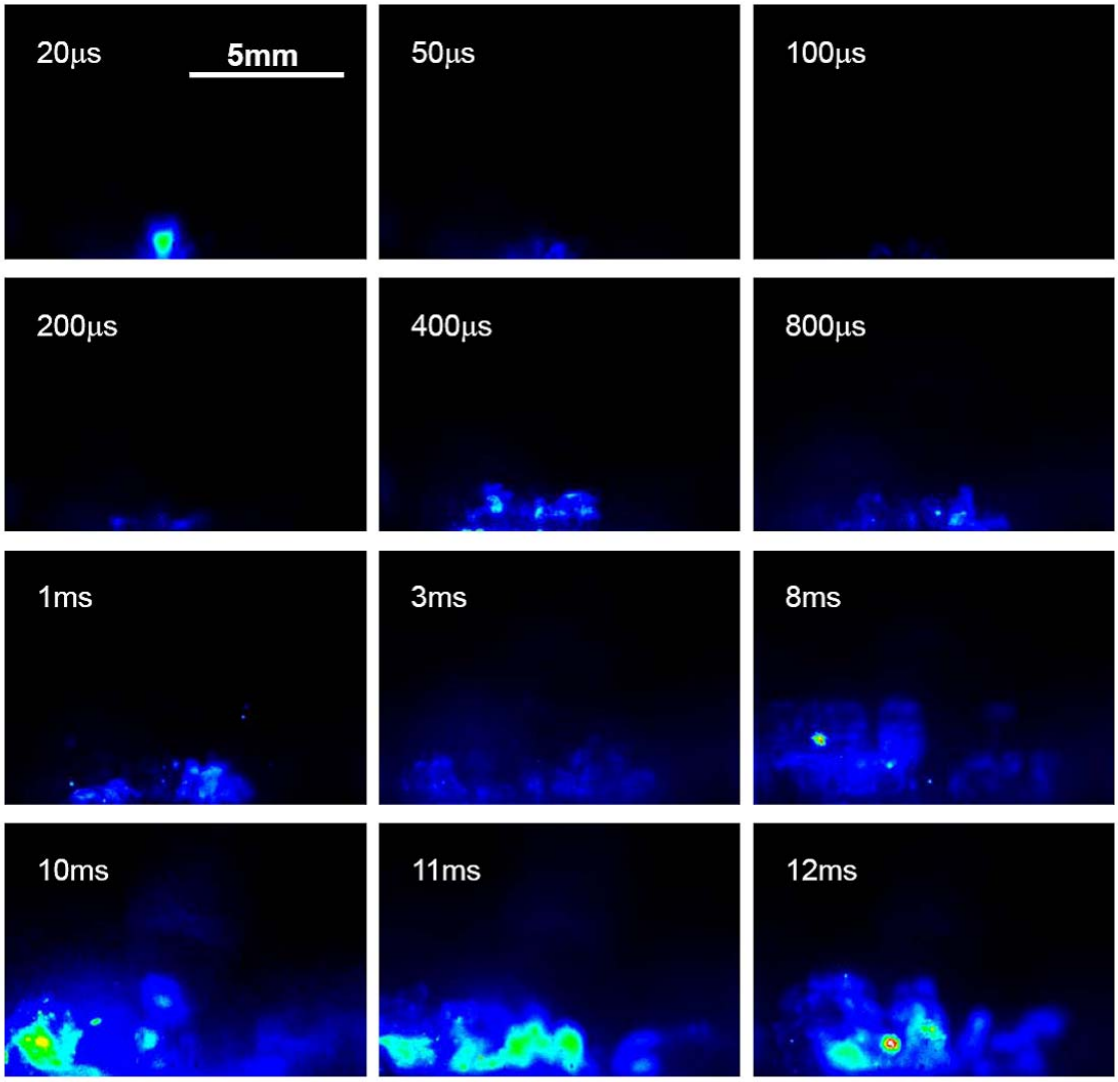
20μs
5mm
50μs
100μs
200μs
400μs
800μs
1ms
3ms
8ms
10ms
11ms
12ms

Figure 7

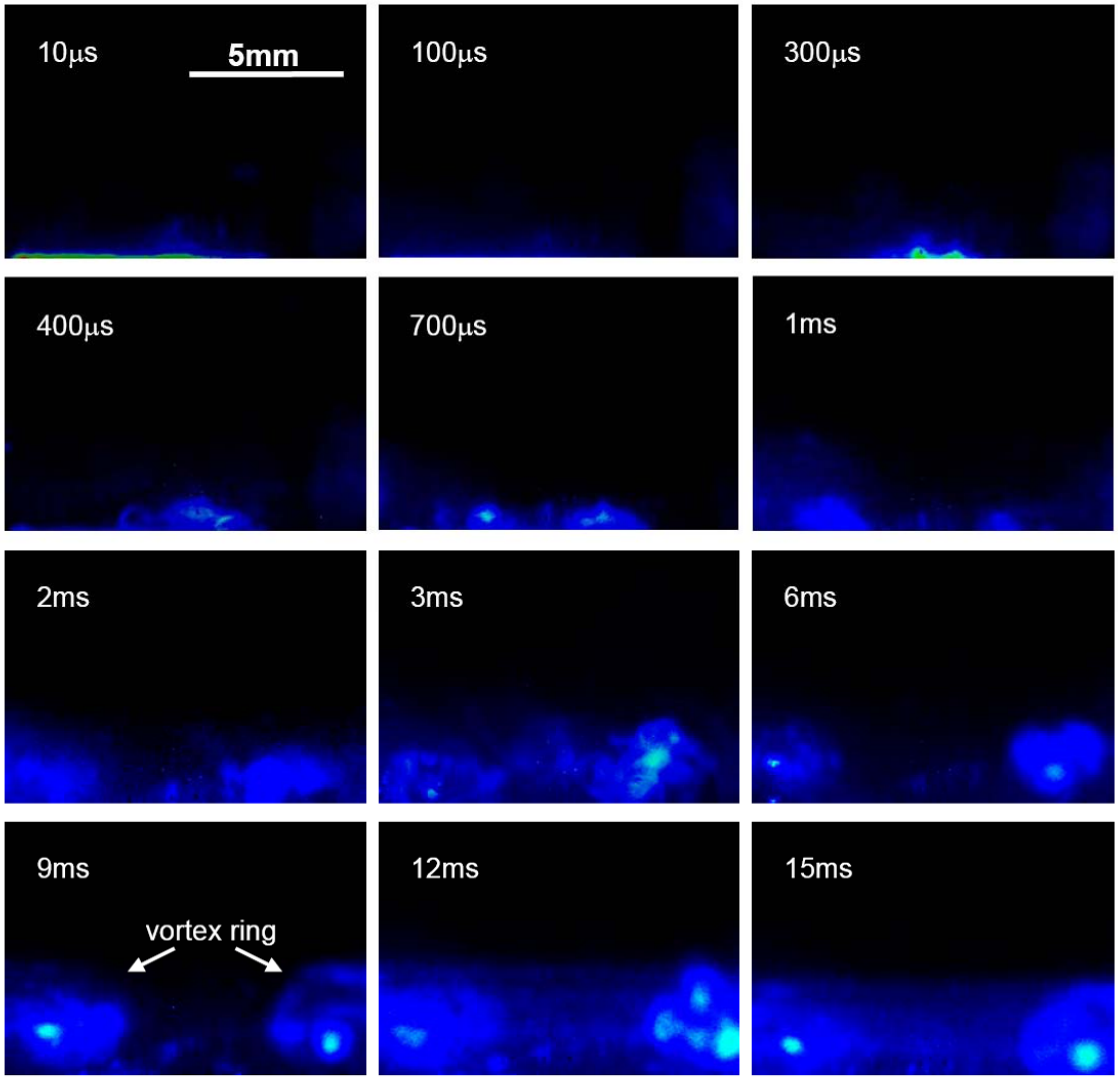
10μs
5mm
100μs
300μs
400μs
700μs
1ms
2ms
3ms
6ms
9ms
vortex ring
12ms
15ms

Figure 8

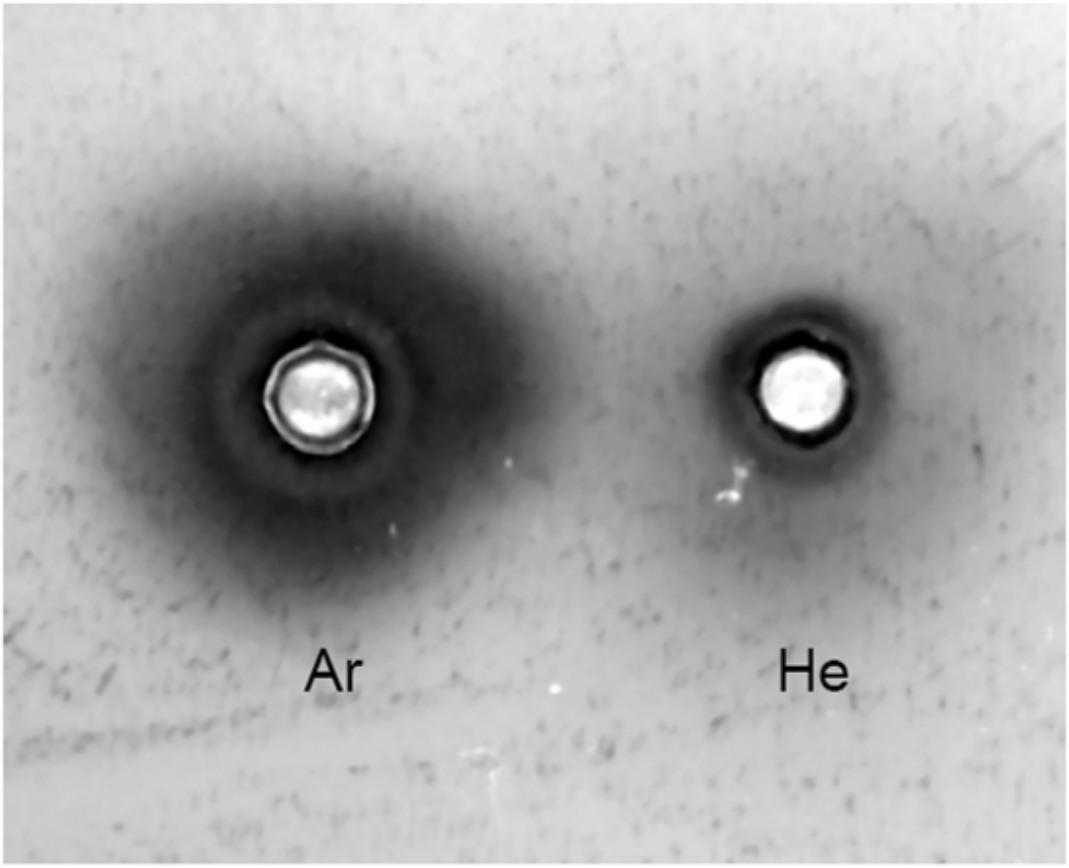

Figure 9

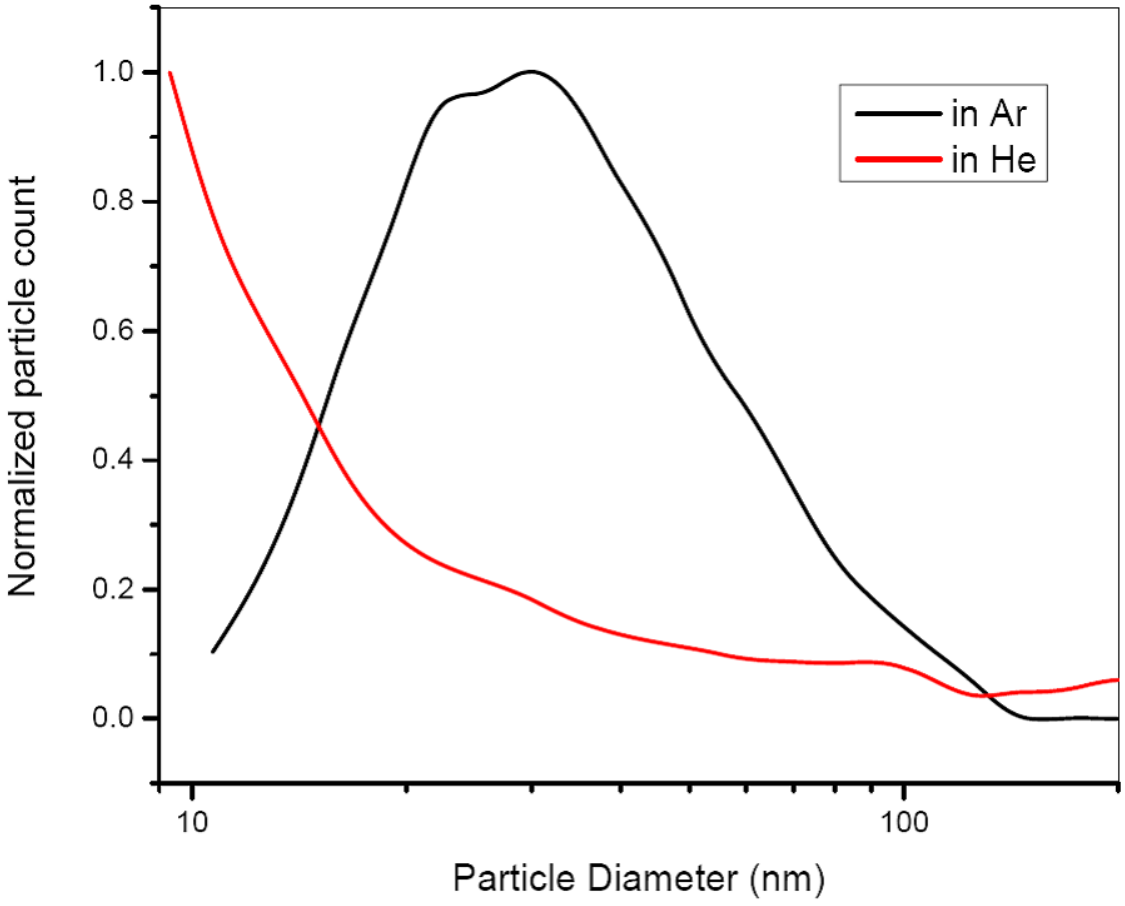
Normalized particle count
1.0
0.8
0.6
0.4
0.2
0.0
10
100
Particle Diameter (nm)
in Ar
in He

Figure 10

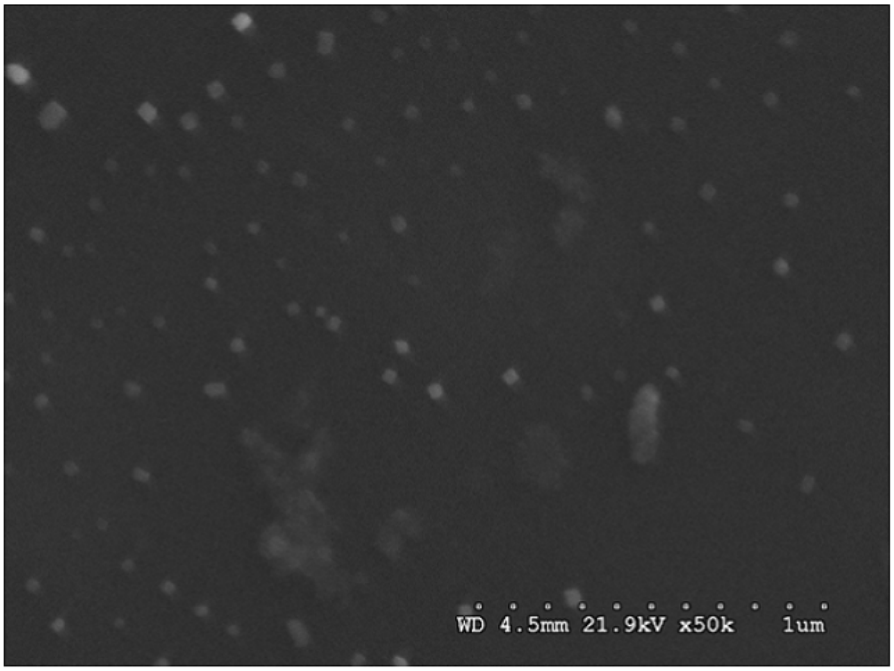
WD 4.5mm 21.9kV x50k 1um

(a)

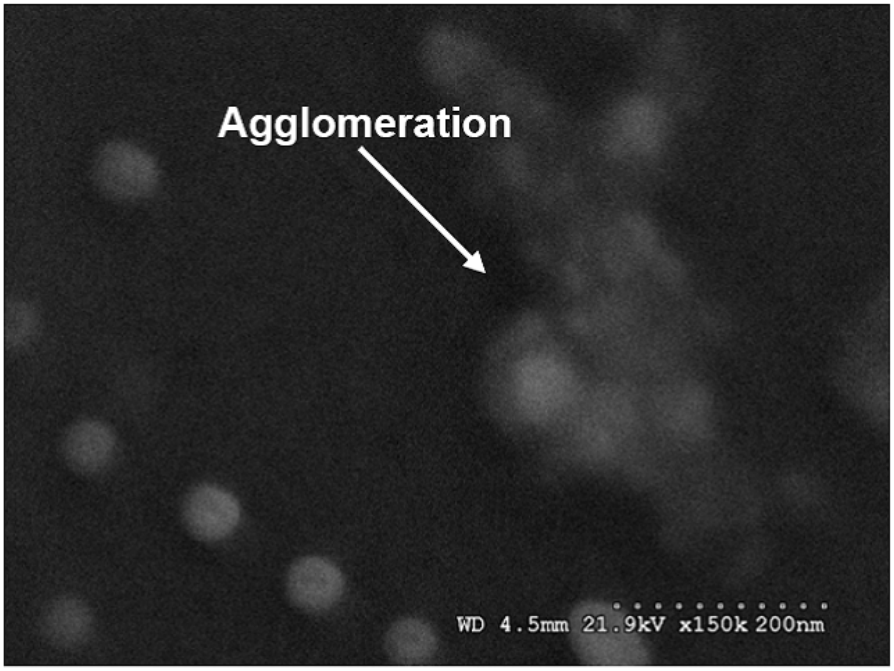
Agglomeration
WD 4.5mm 21.9kV x150k 200nm

(b)

Figure 11

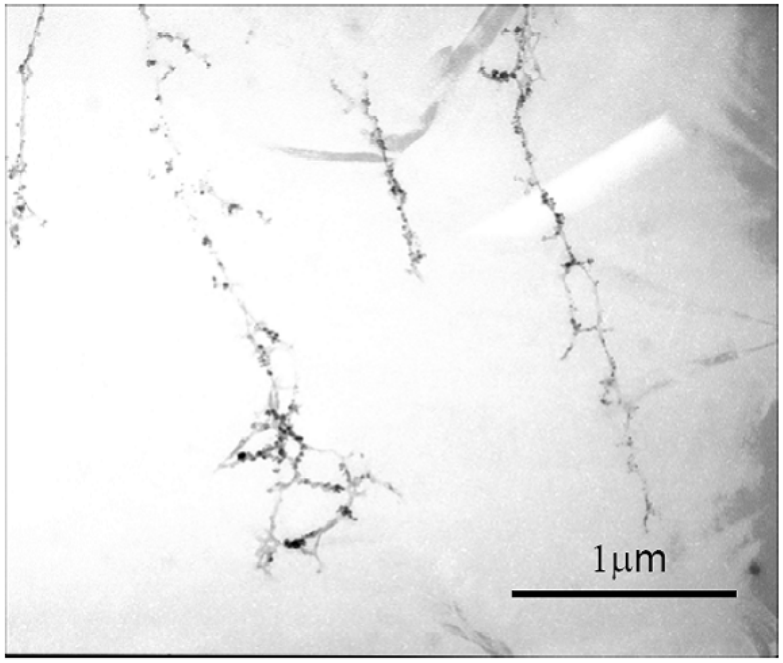

(a)

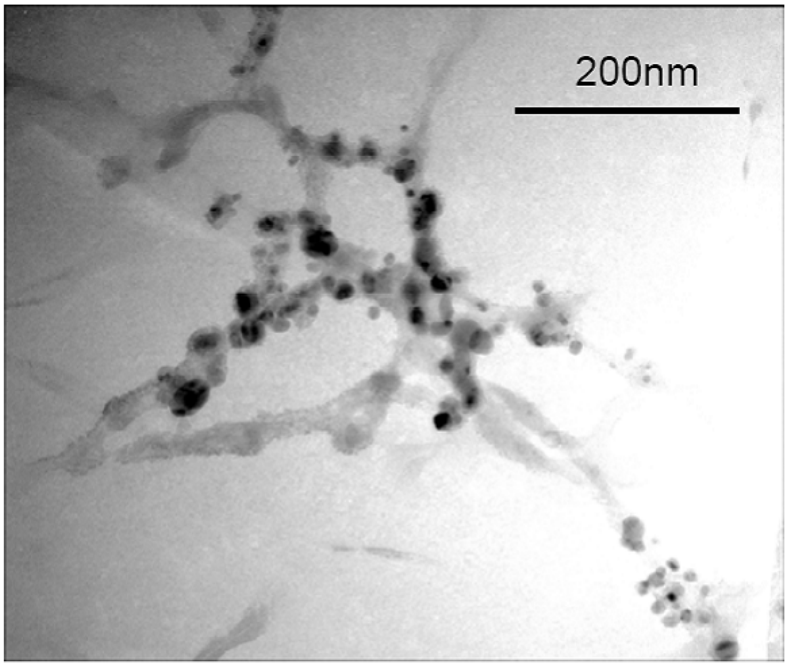

(b)

Figure 12

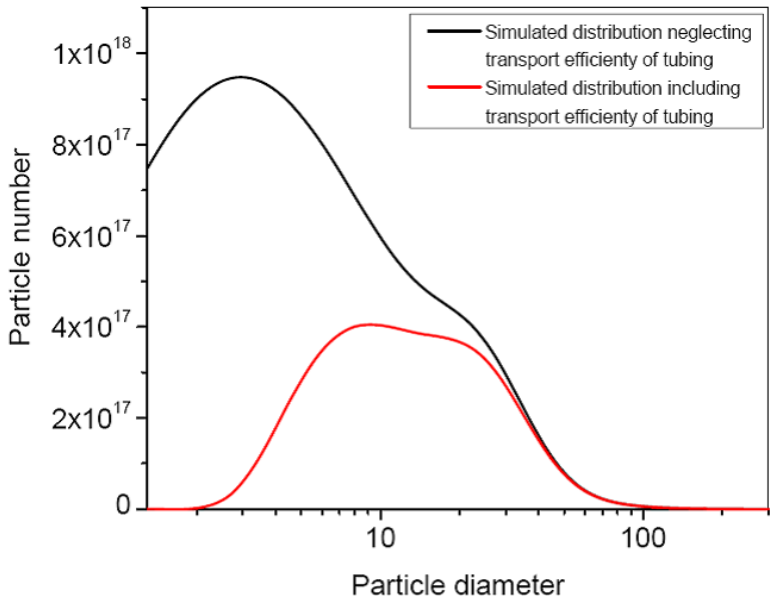
Simulated distribution neglecting transport efficienty of tubing
Simulated distribution including transport efficienty of tubing
Particle number
1x10^18
8x10^17
6x10^17
4x10^17
2x10^17
0
10
100
Particle diameter

(a)

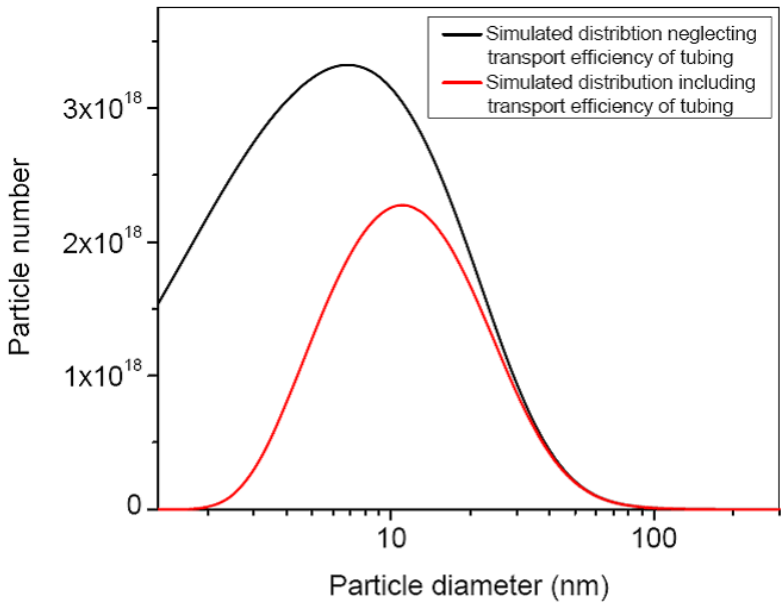
Simulated distribtion neglecting transport efficiency of tubing
Simulated distribution including transport efficiency of tubing
Particle number
3x10^18
2x10^18
1x10^18
0
10
100
Particle diameter (nm)

(b)

Figure 13

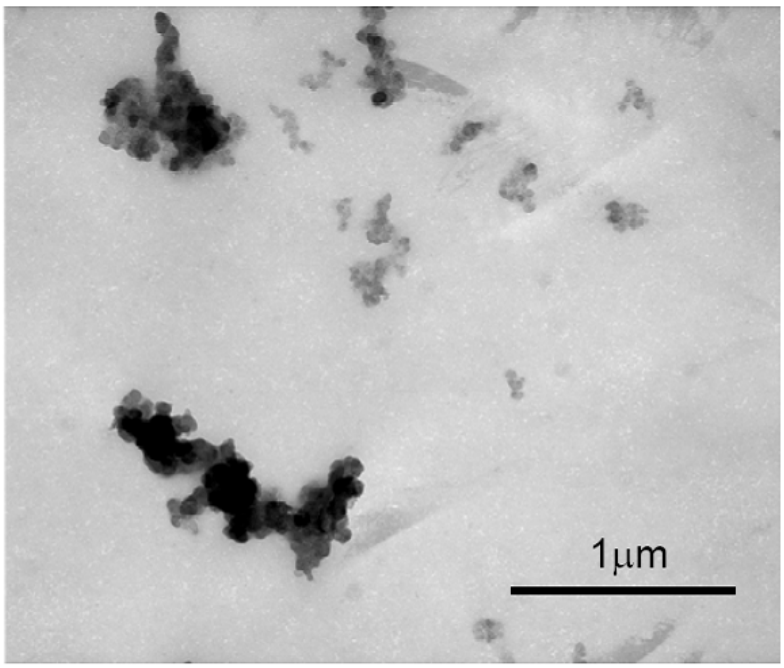

(a)

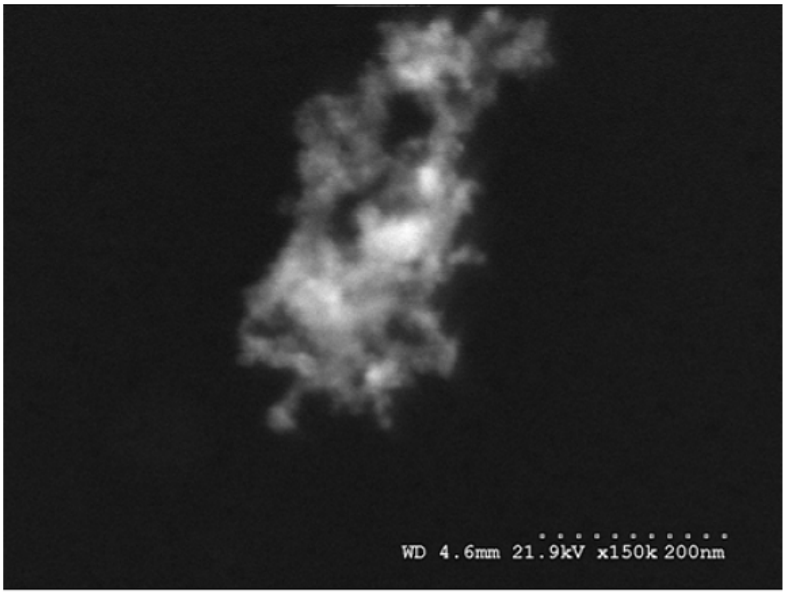

(b)

Figure 14

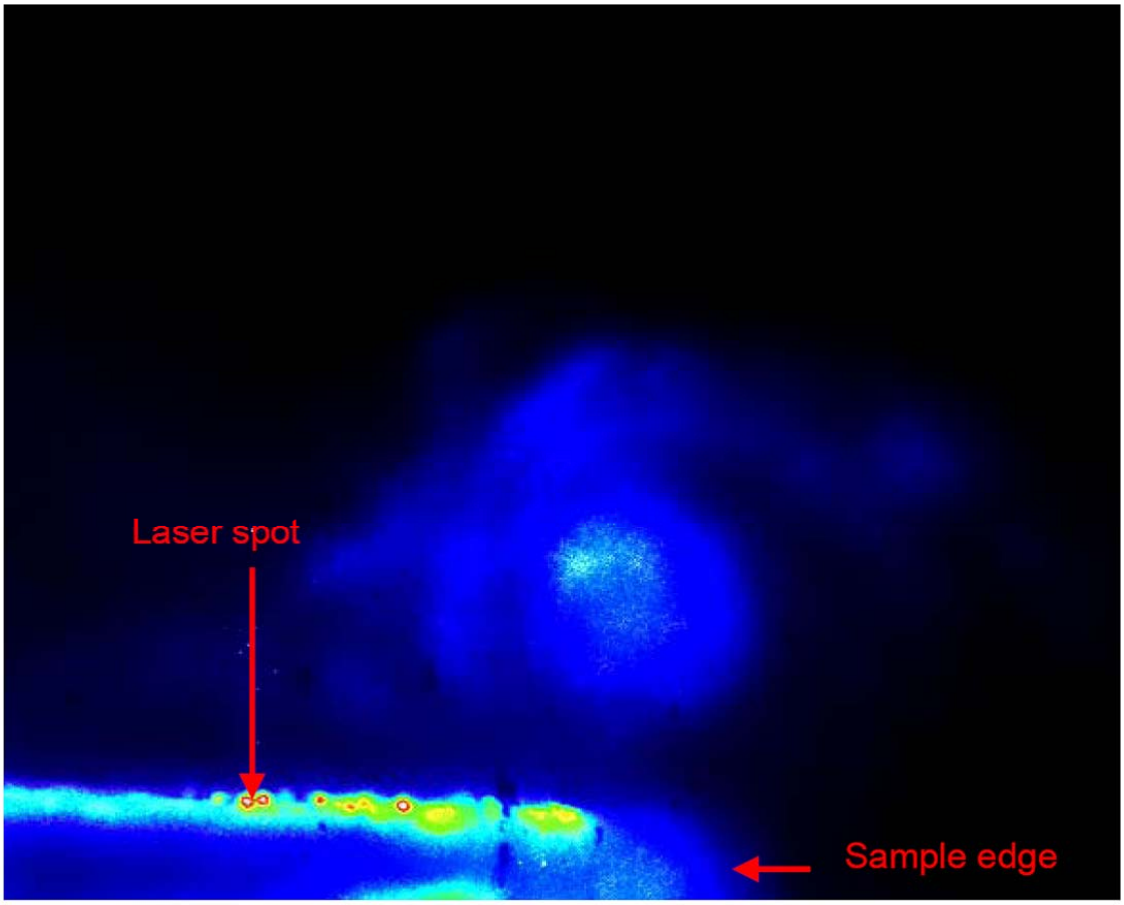

Figure 15

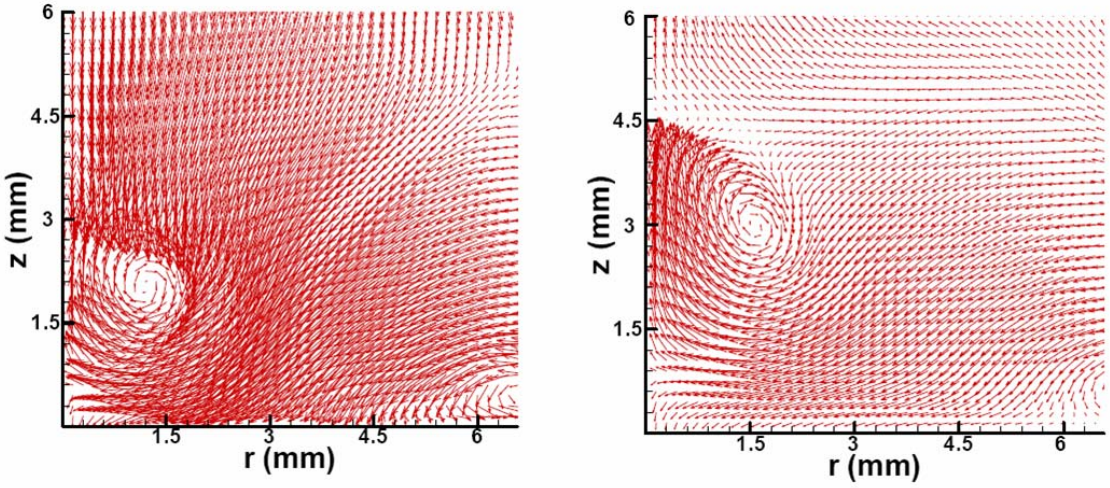

(a) (b)

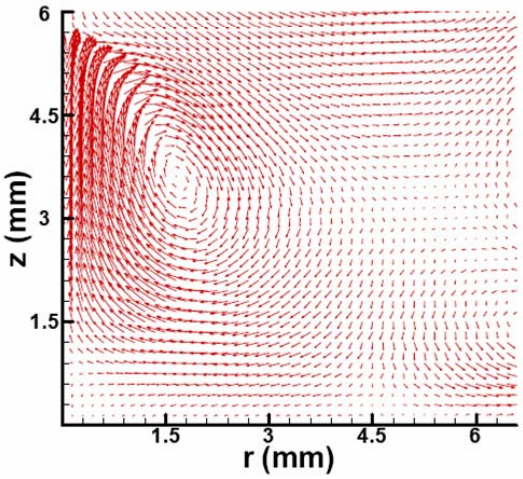

(c)

Figure 16